

Summer@ICERM 2016
RTG “Integrating Dynamics & Stochastics”
I-Team UTRA “Dynamics and Stochastics”

Undergraduate researchers:

Madeline Abbott
Dylan Altshuler
Chloe Avery
Julia Bujalski
Dorothy Catey
Carter Chain
Neil Chandra
Tracy Chin
Cassandra Cole
Jordan Collignon
Surabhi Desai
Philip Doldo
Bethany Dubois
Grace Dywer
Claire Qing Fan
Francesca Lim
Harjasleen Malvai
Melissa Morrissey
Micah Pedrick
Jordan Rosenthal-Kay
Jacob Ruth
Tharathep Sangsawang
Rebecca Santorella
Melissa Stadt
Ryan Utke
Aric Wheeler



Organizers:

Tarik Aougab
Margaret Beck
Paul Carter
Veronica Ciocanel
Todd Kapitula
Quang Nhat Le
Joshua Ruiter
Bjorn Sandstede
Alexandria Volkening



Plurality and Stability in Continuous Time Opinion Formation on Weighted Directed Graphs

Julia Bujalski, Grace Dwyer, Harjasleen Malvai, Jordan Rosenthal-Kay
 Advisor: Todd Kapitula
 TAs: Quang-Nhat Le and Joshua Ruitter

1 Introduction

Ideas that challenge the status quo either evaporate or dominate. The literature that mathematically studies the evolution of ideas treats space as uniform and considers individuals in an isolated community, using an ODE model. We extend these models to include multiple communities and their interaction by using a directed weighted graph. We study in detail some special cases, state general properties, and indicate pathways for further research.

We propose a novel approach in which we account for both local and non-local interactions. We use the model in [1], whose behavior is well understood [2], to understand local interactions, while non-local interactions are governed via a weighted, directed graph. Our model resembles Masuda 2015 [3], in which laws of motion for the probabilities of each individual holding an opinion are derived. However, following Marvel *et al.* 2012 [1], we use a 3-state model of opinion formation. Further, using this 3-state approach, we address the stability of the system when it exhibits *plurality*.

2 The One City Model

Here on, we will refer to these communities as cities. The model presented in [1] is a special case of our model in which there is only

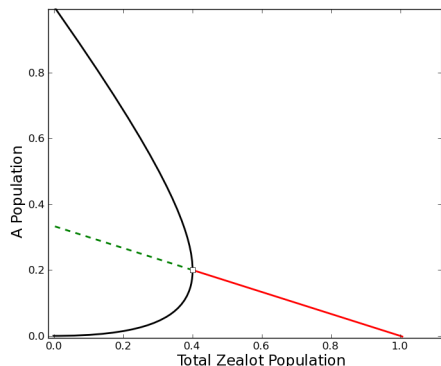


Figure 1: A bifurcation diagram of the system, when varying total zealot population on the x -axis. The solid lines represent stable fixed points, while the dashed lines represent unstable ones.

one city. Here is an overview of this one city case from which we will build our generalization. The model is driven by dyadic (pairwise) interactions between individuals who can hold opinions A , B , or a moderate AB . Additionally, there are committed populations, P of believers of A and Q of believers of B who do not change their opinions. The result of these interactions is governed by the following set of rules:

Speaker	Listener - Preinteraction	Listener - Postinteraction
A, P	B	AB
	AB	A
B, Q	A	AB
	AB	B

Table 1: Rules of interactions

Here, a represents the population proportion of A , likewise b for B , p is the proportion of P , q the proportion of Q . Note that, $m = 1 - a - b - p - q$ is the number of moderates, i.e. the population proportion of those holding opinion AB in the system. We then have the following laws of motion that govern the system, in which the overdot represents differentiation in respect to time

$$\dot{a} = m(p + a) - a(b + q)$$

$$\dot{b} = m(b + q) - b(p + a)$$

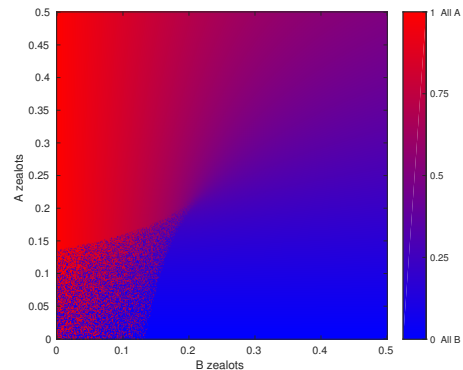


Figure 2: Phase diagram of p vs. q , the figure shows the result of a random initial condition by simulating the system forward in time. The resulting diagram plots the A population (both zealots and non-zealots). Figure 1 corresponds to the line $p = q$

3 The Multi-City Model

The idea is that the influence of any opinion on the people in one community is the weighted average of the influence from every other community and the community on itself. Imagine this weight is encoded by the edge on a graph and the adjacency matrix to this graph is a stochastic matrix. For a community k , we can represent the equations (and interactions with other “ j ” communities) with the following model:

$$\dot{a}_k = m_k \sum_j i_{j,k}(a_j + p_j) - a_k \sum_k i_{j,k}(b_j + q_j) \quad (1)$$

$$\dot{b}_k = m_k \sum_j i_{j,k}(b_j + q_j) - b_k \sum_k i_{j,k}(a_j + p_j) \quad (2)$$

We can write these in matrix notation. In this form the ODEs manifest nonlinearity via a matrix-vector multiplication.

4 The Two-City Case

When investigating the two-city case, we seek to find conditions that evoke plurality. We define plurality as when no opinion is held by 50% or more of the population. Through this analysis we determined that the presence of committed believers does not cause the population to all hold the same opinion but actually creates plurality and allows for coexistence of opinions. Conclusively, committed believers surprisingly act as a moderating force.

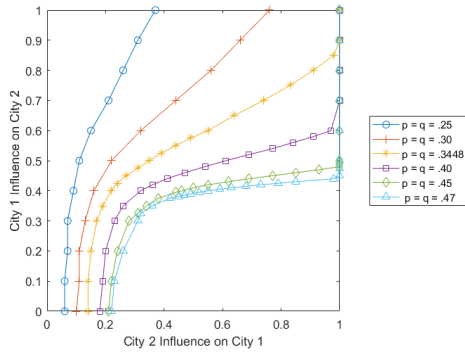


Figure 3: The layout of this scenario is equal populations of A and B committed believers in city 1 and no committed believers in city 2. This graph depicts the nature of behavior of city 1. Each curve represents a different committed believer population. It is clear that as you increase the committed believer population, the ability for the city to reach a pluralistic state increases.

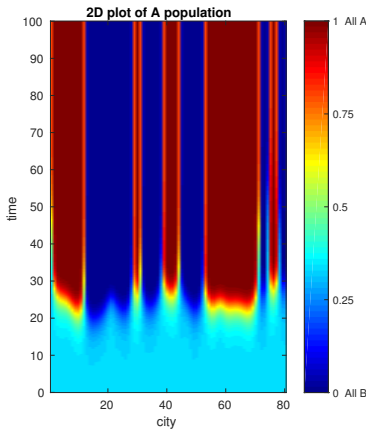
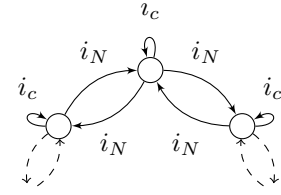


Figure 4: Perturbations around the 1/3 fixed point on the cycle, no hub.

5 Cities on a Cycle

Take a cycle graph. This system is governed by a simple law of motion. The influence factors are denoted i_c and i_N where i_c is a node’s self influence and i_N if the influence a node exerts on their neighbor.



$$\dot{O}_k = \begin{pmatrix} m_k & -a_k \\ -b_k & m_k \end{pmatrix} (i_N \Delta_2 O_k + O_k), \quad k = 1, \dots, N.$$

Where, $2i_N + i_c = 1$ by definition. $O_k = \begin{pmatrix} a_k + p_k \\ b_k + q_k \end{pmatrix}$. And,

$$\Delta_2 O_k = O_{k+1} + O_{k-1} - 2O_k. \quad (3)$$

6 A Cycle Graph With A Hub

A large volume of the literature considers the idea of a dominant voice, like a media, or political figure who is ubiquitous, to whom space does not matter [4, 5, 6, 7]. We introduce this to the cycle graph example by adding a new node, the *hub*, not on the circular graph but connected to every node on the graph.

The law of motion for this new system takes the following form, where c and h subscripts denote the variables belonging to either the *cycle* or the *hub*. If you assume that each node on the cycle is identical, then the collection of nodes on the cycle act then as a single node. This is identically the 2-city case. Note that $2i_N + i_c = (1 - i_{out})$.

$$\begin{aligned} \dot{O}_c &= \begin{pmatrix} m_c & -a_c \\ -b_c & m_c \end{pmatrix} ((1 - i_{out})O_c + i_{out}O_h) \\ \dot{O}_h &= \begin{pmatrix} m_h & -a_h \\ -b_h & m_h \end{pmatrix} ((1 - i_{hub})O_h + i_{hub}O_c) \end{aligned}$$

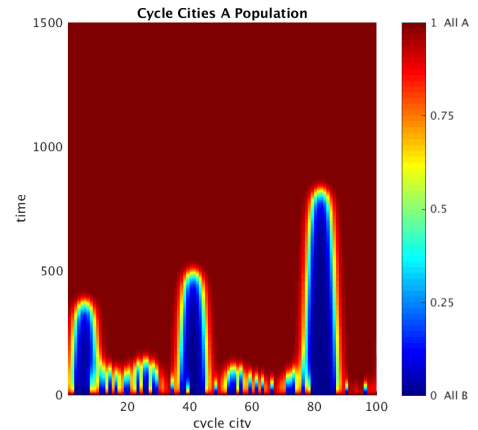


Figure 5: Perturbations on the cycle around the unstable 1/3 fixed point, with hub projecting opinion A.

References

- [1] H. Hong A. Papush S.H. Strogatz Marvel, SA. Encouraging moderation: Clues from a simple model of ideological conflict. *Physical Review Letters*, 2012.
- [2] J Wu S Wang, L Rong. Bistability and multistability in opinion dynamics models. *Applied Mathematics and Computation*, 2016.
- [3] Masuda. Opinion control in complex networks. *New Journal of Physics* 17, 2015.
- [4] B. K. Szymanski P. Singh, S. Sreenivasan and G. Korniss. Competing effects of social balance and influence. *Physical Review E*, 2016.
- [5] Castellano Colaiori. Interplay between media and social influence in the collective behavior of opinion dynamics. *Physical Review E*, 2015.
- [6] Castellano Colaiori. Consensus versus persistence of disagreement in opinion formation: The role of zealots. *Journal of Statistical Mechanics: Theory and Experiment*, 2016.
- [7] C.O. Dorso S. Pinto, P. Balenzuela. Setting the agenda: Different strategies of a mass media in a model of cultural dissemination. *Physica A: Statistical Mechanics and its Applications*, 2016.

Propagation of Lead in Mammals

Melissa Morrissey and Jordan Collignon, Advisor : Todd Kapitula, TA : Veronica Ciocanel
 ICERM : The Institute for Computational and Experimental Research in Mathematics

Lead is ingested into the body in various ways including contaminated air, water, food, soil, and other consumer products [6]. After ingestion, blood takes the lead into the body and then transports it to other tissues and the bones [3]. High amounts of lead released back into the blood can cause lead poisoning which can increase the risk of symptoms such as fatigue, muscle pain, impaired kidney function and inhibited central nervous system [2]. Lead absorption in the skeletal system can also impede bone growth and make the bones brittle. The lead accumulates and can stay in the bone for decades [7].

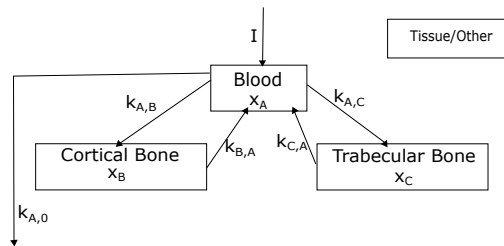


Figure 1: Three-compartment model for dynamics of lead in the body. The I value represents the unknown ingestion rate of lead entering the body and the k values are constants extracted from data in [1].

Using the three-compartment model in figure 1, we considered three differential equations for the dynamics of lead in the body. It was crucial to make the bones into two separate compartments because the tougher cortical bone has a much larger transfer rate from blood to bone than the spongier trabecular bone [1]. Each equation represents the rate at which the amount of lead in the compartment is changing. In order to investigate nonlinearity in our model, the transfer rates from blood to bone and from bone to blood are no longer constant throughout the entire system. We introduced a nonlinear functional form (tanh function) because this was a good fit to the transfer rate curves in [1].

We also used a system of PDEs to describe how lead spreads in a compartment in addition to how lead moves between compartments. This system incorporates diffusion to show how lead spreads in and out of the canalicular region of the bone [5]. The PDE solutions for each compartment are estimated using a Galerkin approximation which transforms the PDE system into a large ODE system. For the model to be accurate, we must also estimate the diffusion rates for both inside and outside of the canalicular region. We considered diffusion rates from [5] and [4] and estimated the diffusion rate for the blood.

By incorporating diffusion and spatial variation in the bone, we observed a more accurate description of the dynamics of lead in the body. Through numerical experiments, we were able to find an estimate of the diffusion in the blood and in the canalicular region. The surface plots in figure 3 show that lead is not distributed uniformly across the bone, but rather lead first starts in the

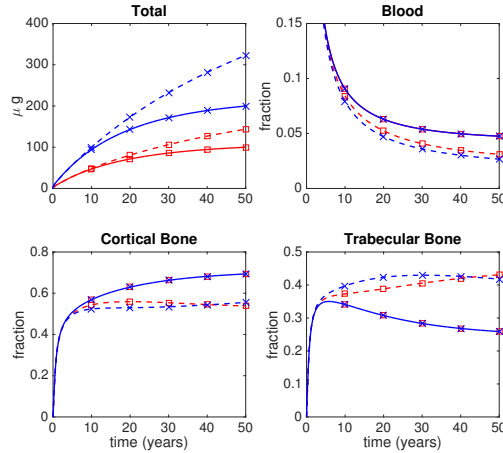


Figure 2: The total amount of lead and the relative percentages of lead in the body. The red curve with squares corresponds to ingestion rate $I = 0.075$ and the blue curve with x's is for $I = 0.15$. The solid lines are calculated using the linear ordinary differential equations, while the dashed lines are calculated using the nonlinear ordinary differential equations.

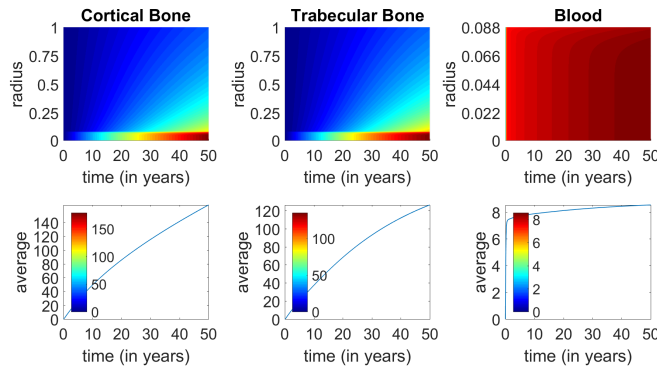


Figure 3: Surface plots for the amount of lead in each compartment are shown in the first row. The spatial averages of lead at each time point for each compartment are shown in the second row.

canalicular territory, then diffuses outward to the rest of the bone. Figure 2 shows the differences in the total amount of lead for the linear and nonlinear systems. It also shows different evolutions of the percentage of lead in the two bones. Our research shows that diffusion and nonlinear factors play an important role in the propagation of lead.

References

- [1] Sepideh Behinaein, David R Chettle, Lesley M Egden, Fiona E McNeill, Geoff Norman, Norbert Richard, and Susan Stever. The estimation of the rates of lead exchange between body compartments of smelter employees. *Environmental Science: Processes & Impacts*, 16(7):1705–1715, 2014.
- [2] Gagan Flora, Deepesh Gupta, and Archana Tiwari. Toxicity of lead: a review with recent updates. *Interdiscip Toxicol*, 5(2):47–58, 2012.

- [3] Todd Kapitula. *Ordinary Differential Equations and Linear Algebra: A Systems Approach*, volume 145. SIAM, 2015.
- [4] Matthew J Kohn and Randolph J Moses. Trace element diffusivities in bone rule out simple diffusive uptake during fossilization but explain in vivo uptake and release. *Proceedings of the National Academy of Sciences*, 110(2):419–424, 2013.
- [5] Allan H Marcus. Multicompartment kinetic models for lead: I. bone diffusion models for long-term retention. *Environmental research*, 36(2):441–458, 1985.
- [6] Michael Rabinowitz. Historical perspective on lead biokinetic models. *Environmental health perspectives*, 106(Suppl 6):1461, 1998.
- [7] Lorentz E Wittmers Jr, Joann Wallgren, Agnes Alich, Arthur C Aufderheide, and George Rapp Jr. Lead in bone. iv. distribution of lead in the human skeleton. *Archives of Environmental Health: An International Journal*, 43(6):381–391, 1988.

Diffusion Maps in Equation-Free Modeling

Paul Carter, Tracy Chin, Jacob Ruth, Björn Sandstede, and Rebecca Santorella

1 Equation-Free Modeling

In many complex dynamical systems, low-dimensional macroscopic behavior emerges from interactions at the high-dimensional microscopic level. Kevrekidis and colleagues have developed a multi-scale approach, called equation-free modeling, to estimate this macro-level behavior through short simulations of the micro-system. The phrase ‘equation-free modeling’ refers to how this method estimates macroscopic variables whose behavior cannot be modeled in an explicit form. This algorithm works through the following three-step process: (1) lift - create initial conditions for the micro-system based on the initial macro-state, (2) evolve - simulate the micro-system for short bursts, and (3) restrict - estimate the macro-state based on the evolution of the micro-state [5, 6]. Not all systems that demonstrate macroscopic behavior are good candidates for equation-free modeling. Ideally, the system should be slow-fast, and the macro-level variables should parametrize the slow manifold.

2 Diffusion Maps

One way to pick out relevant macroscopic variables is to use manifold-learning techniques, which parametrize manifolds based on data from simulations of the underlying system [8]. To parametrize our system, we use diffusion maps, a nonlinear machine-learning technique. This method uses a connection between heat diffusion and random walks to make a Markov transition matrix on the data, with higher transition probabilities between data points that are closer together [1, 2].

A simple example with a swiss roll illustrates how diffusion maps can parametrize a data set [4, 7, 8]. We uniformly sample $m = 1500$ data points given by

$$(x, y, z) = (\theta \cos \theta, \theta \sin \theta, ht), \quad \theta \in [0, 2\pi), t \in [0, 1].$$

Since this data set is clearly parametrized by θ and t , the diffusion map embeds the original three-dimensional data into a two-dimensional manifold given by θ and t .

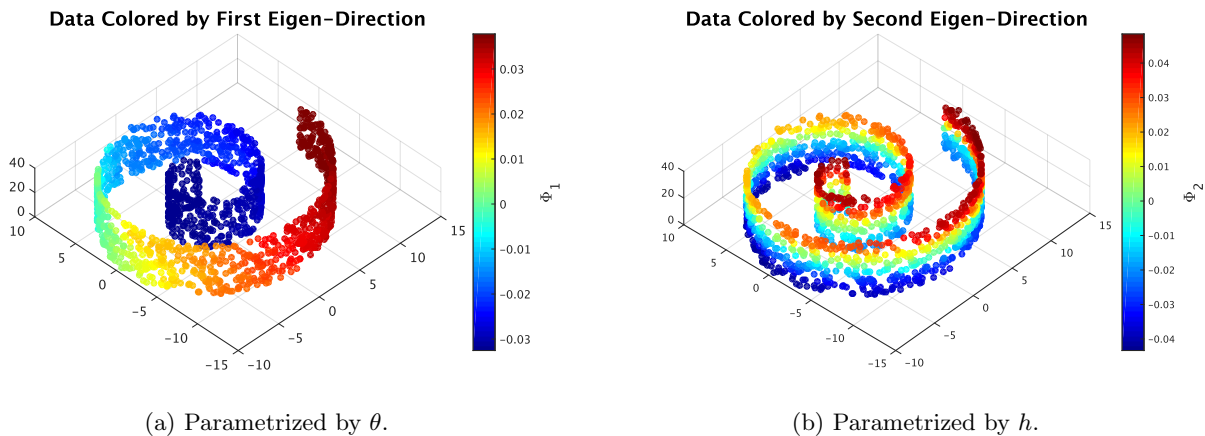


Figure 1: Swiss roll ($h = 40$) colored by the first two distinct eigendirections. Reproduced based on [3, 4].

3 Diffusion Maps and Equation-Free Modeling

In general, equation-free modeling requires problem-specific lifting and restriction operators; however, when using diffusion map embeddings as macroscopic variables, it becomes possible to define more general operators. Previous papers have suggested using the Nyström extension for restriction and simulated annealing for lifting [4, 7]. We find that the Nyström extension efficiently embeds X_{new} into our low dimensional system, but simulated annealing does not yield accurate results.

Instead, we define an implicit scheme to find a lifted profile that is close to a target macro-state and already on the slow manifold. First, we find two microscopic profiles in our data set x_i and x_j with corresponding macro-states ϕ_i and ϕ_j which, after a brief evolution, satisfy the macroscopic condition

$$\phi_i < \phi_{\text{target}} < \phi_j. \quad (1)$$

Then, we build a profile x as a linear combination of x_i and x_j , evolve it briefly, restrict it to ϕ_x , and swap the resulting embedding with either ϕ_i or ϕ_j to ensure that (1) is still satisfied. By repeating this process, we eventually converge upon a lifted profile x that corresponds to ϕ_{target} .

4 Traffic Application

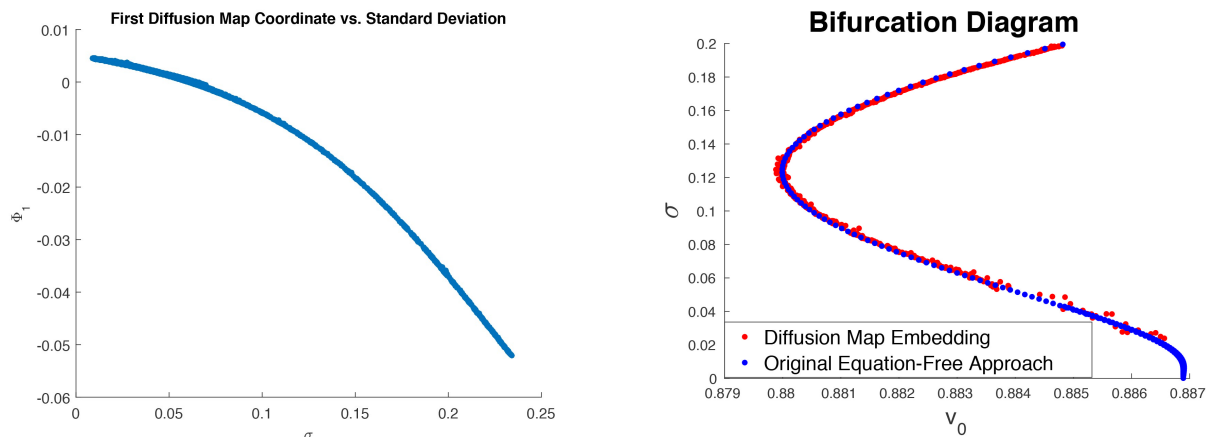
We apply equation-free modeling to a system of n cars driving around a ring road of length L from [9]. All cars follow uniform, deterministic behavior governed by:

$$\tau \ddot{x}_i + \dot{x}_i = V(\Delta x_i), \quad i = 1, 2, \dots, n, \quad (2)$$

where τ is the inertia, x_i is the position, Δx_i is the headway, and V is the optimal velocity function:

$$V(\Delta x_i) = v_0(\tanh(\Delta x_i - h) + \tanh(h)). \quad (3)$$

Based on the parameter v_0 and initial conditions, two patterns can emerge: free-flow or traffic jams. In [9], Marschler et al. use the standard deviation of the headways (σ) as their macroscopic variable to classify traffic behavior. We use diffusion maps to verify σ as an appropriate macroscopic variable. In Figure 2a, the diffusion map embedding is plotted against the standard deviation of the headways. Since the macroscopic variables Φ_1 and σ clearly have a one-to-one relationship, the diffusion map verifies σ as a good choice.



(a) Φ_1 has a one-to-one relationship with σ

(b) The top branch corresponds to stable jams and the lower branch to unstable jams.

Figure 2: Comparison of the equation-free methods in σ and in Φ_1 .

We reproduce the bifurcation diagram presented in [9], but using only diffusion map coordinates and the lifting and restricting operators defined above (Figure 2b). Although the bifurcation diagram produced by the diffusion map embedding follows the same general trajectory, it is significantly less precise due to errors in lifting and restricting as well as the sparsity of our data around the unstable lower branch.

5 Conclusions

When the presence of an underlying slow manifold is known, diffusion maps can be a valuable tool for identifying useful parametrizations; however, further work must be done to improve the utilization and accuracy of diffusion map based operators in equation-free modeling.

References

- [1] Ronald R Coifman and Stéphane Lafon. “Diffusion maps”. In: *Applied and computational harmonic analysis* 21.1 (2006), pp. 5–30.
- [2] Ronald R Coifman et al. “Geometric diffusions as a tool for harmonic analysis and structure definition of data: Diffusion maps”. In: *Proceedings of the National Academy of Sciences of the United States of America* 102.21 (2005), pp. 7426–7431.
- [3] Carmeline J Dsilva et al. “Parsimonious representation of nonlinear dynamical systems through manifold learning: A chemotaxis case study”. In: *Applied and Computational Harmonic Analysis* (2015).
- [4] Radek Erban et al. “Variable-free exploration of stochastic models: a gene regulatory network example”. In: *The Journal of chemical physics* 126.15 (2007), p. 155103.
- [5] Ioannis G Kevrekidis, C William Gear, and Gerhard Hummer. “Equation-free: The computer-aided analysis of complex multiscale systems”. In: *AIChE Journal* 50.7 (2004), pp. 1346–1355.
- [6] Ioannis G Kevrekidis and Giovanni Samaey. “Equation-free multiscale computation: Algorithms and applications”. In: *Annual review of physical chemistry* 60 (2009), pp. 321–344.
- [7] Carlo R Laing, Thomas A Frewen, and Ioannis G Kevrekidis. “Coarse-grained dynamics of an activity bump in a neural field model”. In: *Nonlinearity* 20.9 (2007), p. 2127.
- [8] Christian Marschler et al. “Coarse-grained particle model for pedestrian flow using diffusion maps”. In: *Physical Review E* 89.1 (2014), p. 013304.
- [9] Christian Marschler et al. “Implicit methods for equation-free analysis: convergence results and analysis of emergent waves in microscopic traffic models”. In: *SIAM Journal on Applied Dynamical Systems* 13.3 (2014), pp. 1202–1238.

Summary of Koopman Theory Results

Carter Chain, Micah Pedrick, Ryan Utke

Set-up

We explored the Koopman operator, specifically the relationships between stability, eigentheory, and observable space. Given some dynamical system

$$x_{k+1} = F(x_k)$$

and a space of observables $\mathcal{F} : K \rightarrow K$, the Koopman operator $U : \mathcal{F} \rightarrow \mathcal{F}$ is defined by $U(g) = g \circ F$. This gives the analogue of the dynamical system in observable space, with the hope that these "observable dynamics" are connected to the original dynamics of interest. Our general results are as follows, glossing over some technical assumptions and the like:

Construction of eigenfunctions

We can construct an eigenfunction for simple one-dimensional dynamics when $|\lambda| < 1$. The construction relies on first finding a fundamental domain on which to define a function, then propagating this domain through the dynamics, scaling by λ each iteration. This also indicates the importance of the observable space, as different observables give different restrictions of the function behavior on the fundamental domain.

We can construct a continuous eigenfunction for any unique globally stable or unstable fixed point or limit cycle. In fact, the construction generalizes to stable or unstable fixed points in any system, again assuming uniqueness of the attractor: take some surface around the fixed point, and its image under the dynamics. This bounds some region to be used as the fundamental domain, which then defines the behavior of any eigenfunction. This generalizes even further to limit cycles, where taking a surface around one point of the cycle and its image under the n th iterate of the dynamics (for n the period of the cycle) to bound the fundamental domain.

We established a relationship between the rates of convergence and divergence of equilibria and the L^2 eigenvalues. In particular, the rate of convergence to an attractor determines a maximum (possibly infinite) spectral radius, while the rate of divergence from an unstable equilibrium determines a minimum (possibly zero) radius. The relationship arises through integrability requirements: sufficiently fast convergence to an attractor of the system can make the eigenfunctions corresponding to eigenvalues of modulus greater than one diverge slowly enough to be integrable, and similar arguments hold for unstable equilibria. Subexponential convergence or divergence results in a maximum or minimum spectral radius of 1, respectively. Exponential convergence or divergence sets a bound a positive distance away from 1, determined by the base of the exponential, which is not attained. Superexponential convergence results in all complex values of modulus greater than 1 being eigenvalues; superexponential divergence allows all complex values with modulus less than 1. This means that the L^2 spectrum is typically an annulus in the complex plane.

Numerical Approximations

Spectra converge slowly using typical finite-difference methods. In a naive scheme (partition the interval into equidistant points, approximate the Koopman operator by an operator on \mathbb{R}^n), the spectrum included 1, some spurious values depending on the system (for instance, with $x_{k+1} = 0.8x_k$, 0.8 is an eigenvalue), and a disc centered at the origin. As we increase the partition size, this disc should expand to fill the entire interval. In the linear case, convergence is unclear, certainly slow, while for say the quadratic case the approximated spectrum does not seem to converge to the unit disc at all, certainly not quick enough to be practical.

Pseudospectra, which converge rapidly, are a practical alternative. To deal with these problems, we turn to the pseudospectrum, which allows ends up converging to the full unit disc quite quickly. Pseudospectra are related to the size of the resolvent norm, or rather how non-normal an operator is. In a system with a 2-cycle, we see an eigenvalue of -1 , while in a system with a 3-cycle we see eigenvalues $e^{\frac{2\pi i}{3}}$. Around -1 , we see the resolvent norm is large, and the (approximation of the) Koopman operator is non-normal, but around $e^{\frac{2\pi i}{3}}$ we see different behavior depending on the chaotic behavior of the system. In one example, where the chaos is restricted to a measure 0 set, the Koopman operator is non-normal around $e^{\frac{2\pi i}{3}}$ as expected. However, in another example, wherein the 3-cycle was surrounded by chaos, the Koopman operator was normal around $e^{\frac{2\pi i}{3}}$, with no apparent increase in resolvent norm.

Miscellany

We explored some generalized eigentheory. We explicitly found generalized eigenfunctions for linear dynamics and $C^0(\Omega)$ observables. In this case, there is an infinite chain of generalized eigenfunctions for all proper eigenfunctions with eigenvalue of modulus strictly less than 1. These are in a sense generated by the logarithm function, with each n th order generalized eigenfunction in the chain being a product of the proper eigenfunction and a degree n polynomial in the logarithm. It seems like this "generator" mechanism may be present in other dynamics. Since imposing differentiability requirements shrinks the disc of eigenvalues within which eigenfunctions have generalized eigenfunction families in the linear scheme, the relationship between $C^k(\Omega)$ and generalized eigentheory seems worth investigating.

Project Summary: Nonorientable Bundles

Surabhi Desai, Melissa Stadt, and Aric Wheeler

Mentors: Margaret Beck and Björn Sandstede

TAs: Tarik Aougab and Paul Carter

August 18, 2016

1 Project Description

The goal of our project was to build on the study of localized roll solutions by considering systems with nonorientable stable and unstable manifolds of the periodic orbit. We considered the system of ordinary differential equations

$$u_x = f(u, \mu), \quad u \in \mathbb{R}^4, \quad \mu \in \mathbb{R} \quad (1.1)$$

in \mathbb{R}^4 , where f is some smooth function with a parameter μ . Localized roll solutions are solutions that start from some steady state to an oscillatory state for some time then return to the steady state. Figure 1.1 shows an example of a localized roll solution in phase space.

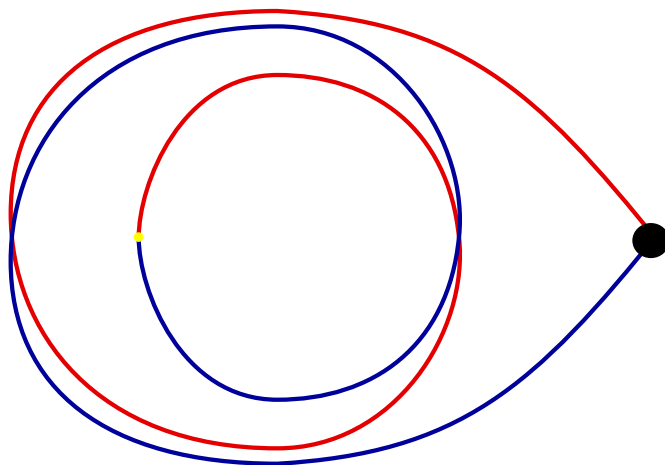


Figure 1.1: Example of gluing in phase space in \mathbb{R}^3 . The red trajectory represents a front and the blue trajectory represents a back that travel from the equilibrium around the green periodic orbit then are glued at the yellow point, creating a localized roll solution.

1.1 Background

In the system (1.1) there is assumed to be a periodic orbit, γ , and two-dimensional stable and unstable manifolds of the periodic orbit. The stable manifold of γ , $W^s(\gamma, \mu)$ has a flow that attracts solutions towards the periodic orbit. Similarly the unstable manifold of γ , $W^u(\gamma, \mu)$ has

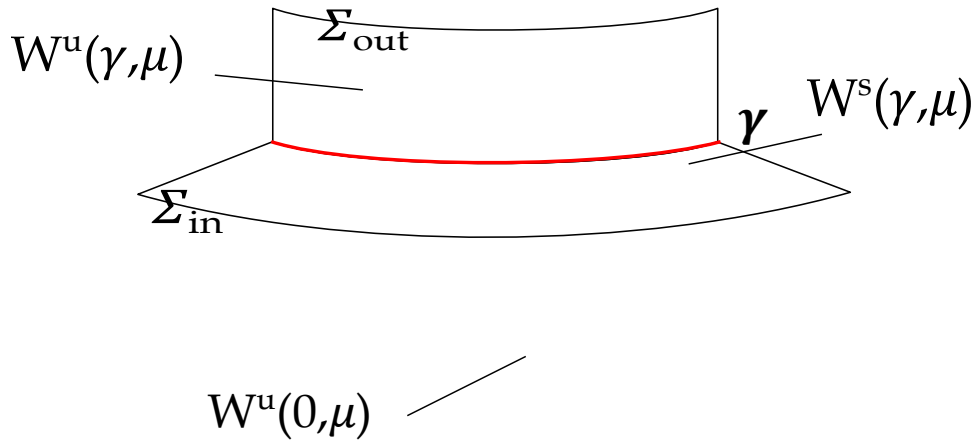


Figure 1.2: An illustration of a piece of the system near the periodic orbit (red) and the unstable and stable manifolds of the periodic orbit. The sections Σ_{in} and Σ_{out} are in gray at distance $\delta > 0$ from the periodic orbit along the respective manifold. In green we have the unstable manifold of the equilibrium intersecting Σ_{in} . By reversibility the stable manifold of the equilibrium will intersect Σ_{out} and return to the equilibrium, but is not included in this illustration for clarity.

a flow that repels solutions away from the periodic orbit. To study the solution types we change the coordinate system to a system called Fenichel coordinates which straighten out the stable and unstable manifolds of γ . In the analysis, in order to determine when a solution enters the region of the periodic orbit we define Σ_{in} and Σ_{out} which are sections that are $\delta > 0$ distance from γ perpendicular to $W^s(\gamma, \mu)$ and $W^u(\gamma, \mu)$ respectively as shown in Figure 1.2. There are also unstable and stable manifolds of the equilibrium, $u = 0$, $W^u(0, \mu)$ and $W^s(0, \mu)$ respectively. The stable manifold of the equilibrium encodes all the trajectories that leave the δ region that is defined by Σ_{out} and return to the equilibrium. Figure 2.5 shows an illustration of a system that is orientable and was studied in [1].

1.2 Nonorientable Bundles

Our project was to study how solutions in the orientable system change when the stable and unstable manifolds of the periodic orbit are nonorientable. Since the stable and unstable manifolds of the periodic orbit are two dimensional, they become Möbius bands as shown in Figure 1.3.

2 Results

The types of intersections of Σ_{out} and $W^u(0, \mu)$ are important in determining the types of localized roll solutions found in the system. These intersections are encoded in a set defined as

$$\Gamma := \{(\varphi, \mu) \in \mathbb{S}^1 \times J : W^s(0, \mu) \cap W^{uu}(\gamma(\varphi, \mu), \mu) \cap \Sigma_{out} \neq \emptyset\}, \quad \mathbb{S}^1 = [0, 4\pi] / \sim.$$

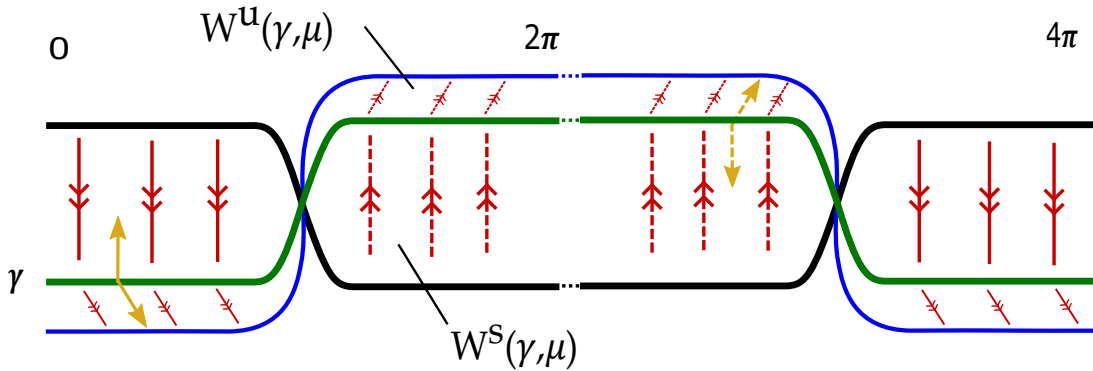


Figure 1.3: An illustration of Möbius band stable and unstable manifolds of the periodic orbit. We must consider 4π -periodicity in order to match the vector directions so we visualize the stable and unstable manifolds of the periodic orbit as two Möbius bands glued together. The red arrows indicate the general direction of the flow on the respective invariant manifold to the periodic orbit depicted in green. The black and blue edges of the manifolds are where Σ_{in} and Σ_{out} are respectively. In yellow are the examples of the $p^s(x, \mu)$ and $p^u(x, \mu)$ vectors with the condition of changing directions after 2π .

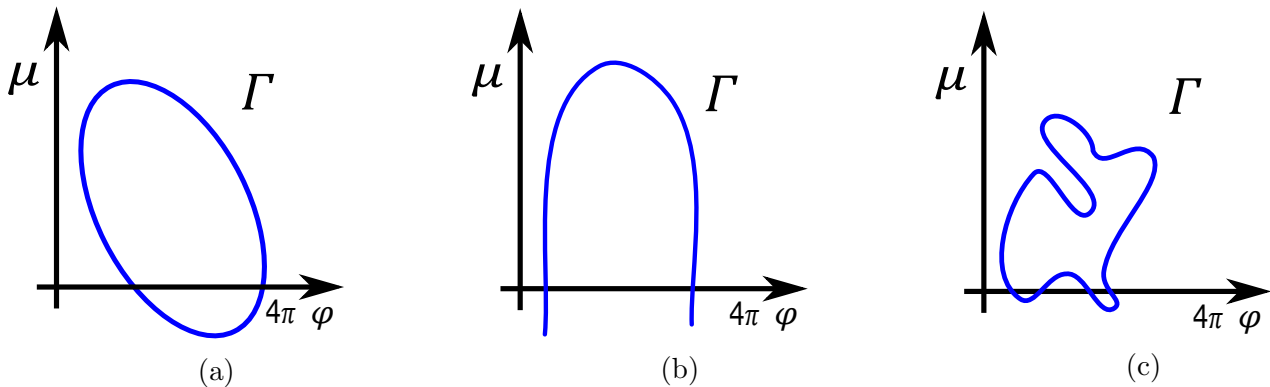


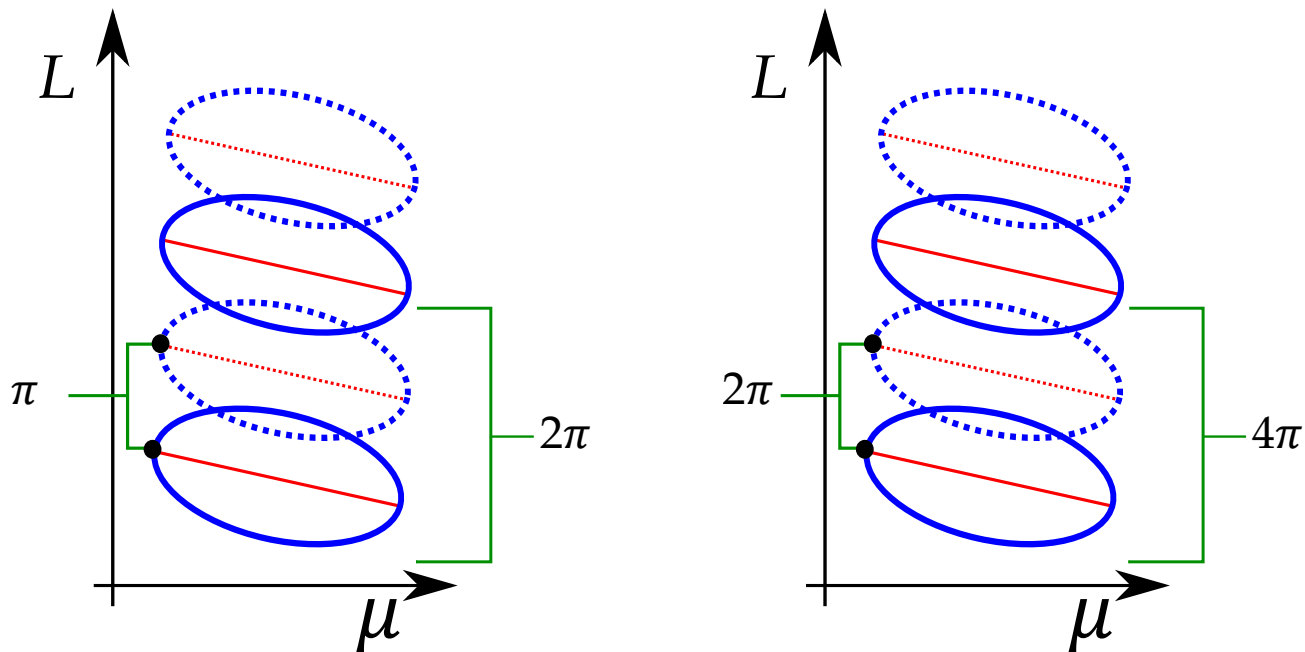
Figure 2.1: Examples of isola intersections.

2.1 Isolas

An isola is a local intersection that is path homotopic to a point when considering the space Σ_{out} . An isola can be any intersection that does not intersect for some $\varphi \in [0, 4\pi]$. The solutions for isolas are very similar to those of the orientable case because of the local geometry. There is a change in the distance between saddle nodes in the bifurcation diagrams as shown in Figure 2.2. In Figure 2.1 some examples are illustrated to show what the isola intersections may look like.

2.2 Global Intersections

A global intersection is an closed curve that is not contractible on Σ_{out} . Therefore a global intersection intersects at every $\varphi \in [0, 4\pi]$. In the orientable case of (1.1), these intersections lead to snaking behavior in the bifurcation diagrams which is a characteristic of interest in the study of localized roll solutions. An example of snaking behavior in a bifurcation diagram is given in Figure 2.4. We found in the nonorientable case that these intersections are not possible due to linking of the boundary of the Möbius band $W^s(\gamma, \mu)$ and the periodic orbit, hence snaking does not occur. This result was generalized to systems with twisted invariant manifolds of the periodic orbit.



(a) An example of a bifurcation diagram of isola intersections in the orientable cylindrical system.

(b) An example of a bifurcation diagram of isola intersection in the nonorientable Möbius system.

Figure 2.2: An example of the isola bifurcation diagrams for an orientable and nonorientable system. The vertical axis L measures the “time” x spent by the homoclinic orbit near the periodic orbit γ so is about equivalent to the L^2 -norm of the corresponding localized state. The ellipsoids correspond to the symmetric pulses and the horizontal branches correspond to the asymmetric pulses. The solid lines and dotted lines correspond to different values of φ_0 . Note that the distances between the isolas in the nonorientable system bifurcation diagram is double the distance between isolas in the orientable system.

3 Acknowledgments

We would like to thank Prof. Margaret Beck, Prof. Björn Sandstede, Dr. Tarik Aougab and Dr. Paul Carter for their invaluable support and guidance in this project. We would also like to thank ICERM for giving us this opportunity and providing a wonderful research environment with a lovely view. This project was funded by the NSF and ICERM.

References

[1] Margaret Beck, Jürgen Knobloch, David J. B. Lloyd, Björn Sandstede, and Thomas Wagenknecht. Snakes, ladders, and isolas of localized patterns. *SIAM J. Math. Anal.*, 41(3):936–972, 2009.

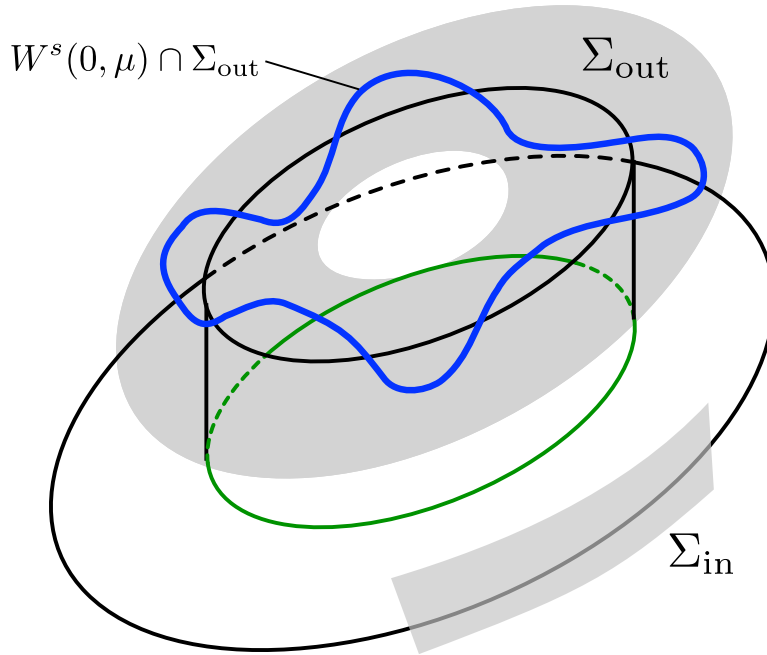


Figure 2.3: An illustration of a global intersection. The gray annulus is Σ_{out} with the blue curve showing the intersection of the stable manifold of the equilibrium and Σ_{out} . Note that there will also be a global intersection by reversibility in Σ_{in} .

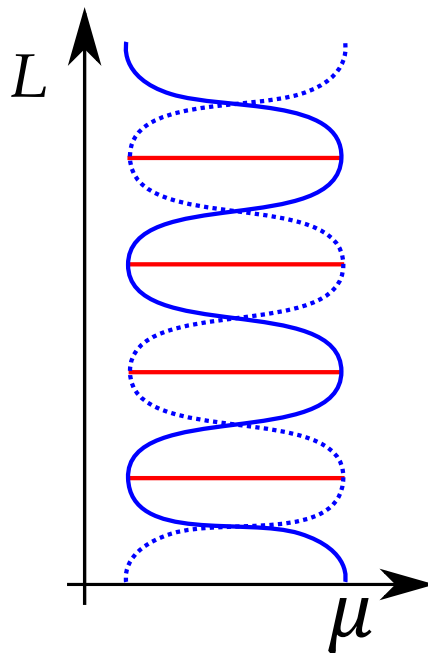


Figure 2.4: An example of a bifurcation that includes the characteristic bifurcation curve behavior of snaking. Snaking is when there are two intertwining wiggly curves and was observed for global intersections of the cylindrical case.

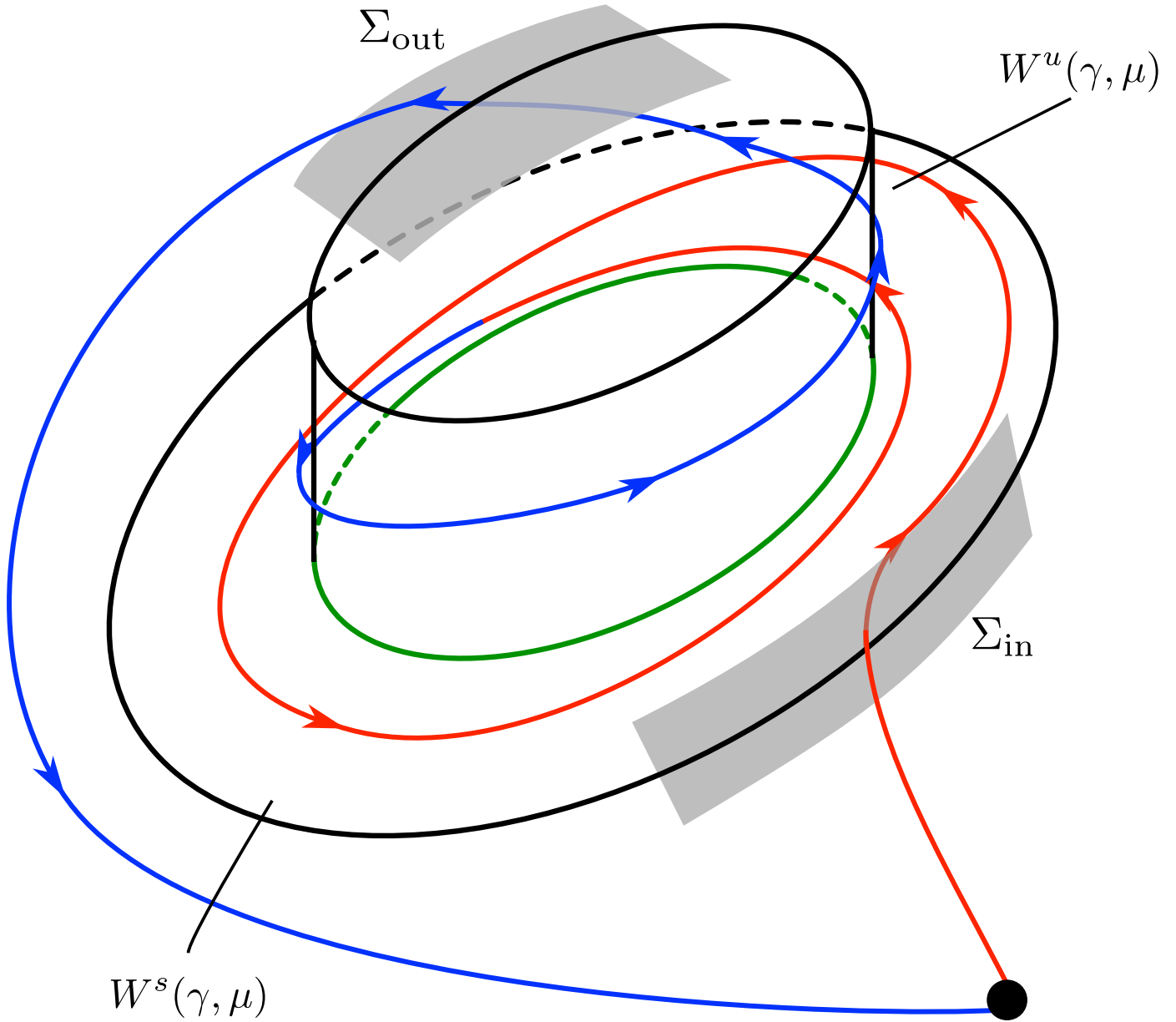


Figure 2.5: A three-dimensional schematic view of the gluing construction on the system with positive Floquet multipliers thus a topologically cylindrical surface. The green circle is the periodic orbit. The gray sections are parts of Σ_{in} and Σ_{out} as labeled. Note that in the system, Σ_{in} and Σ_{out} go all the way around the cylinder and annulus, but this is not drawn here for clarity. The red line is a front that in forward time go through Σ_{in} near $W^s(\gamma, \mu)$ around the periodic orbit. The blue line is a back that in backward time goes through Σ_{out} near $W^u(\gamma, \mu)$ to the periodic orbit. The front and back and shown to be glued to show a localized roll solution for this system.

Snaking in the Swift-Hohenberg Equation in Dimensions 1 Versus $1+\varepsilon$

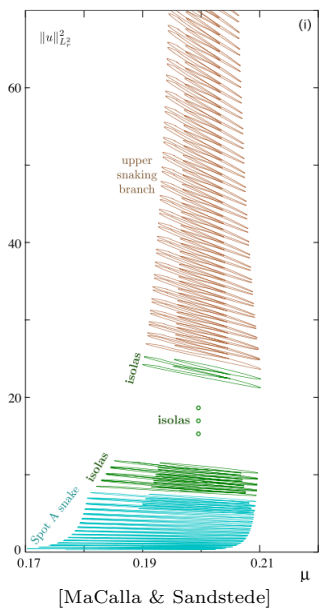
Dylan Altschuler ^{*} Chloé Avery [†] Tarik Aougab [‡] Margaret Beck [§] Paul Carter [‡]
 Björn Sandstede [‡] Tharathep Sangsawang [¶]

August 12, 2016

The Swift-Hohenberg equation (1) is a widely studied non-linear partial differential equation that can describe many spatially-localized structures. Spatially-localized structures occur in the natural world, such as in vegetation patterns [6, 7] and crime hotspots [3].

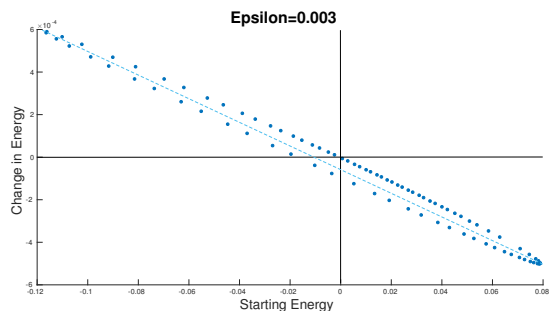
$$u_t = - \left(1 + \frac{n-1}{x} \partial_x + \partial_{xx} \right)^2 u - \mu u + \nu u^2 - u^3 \quad (1)$$

The bifurcation structure of the one-dimensional Swift-Hohenberg equation exhibits a phenomenon called snaking. That is, solutions bounce between two different values of a parameter, μ , while moving up in the L^2 -norm. The mechanism that creates snaking in the one-dimensional case is well-understood [1, 2, 4]. However, numerical studies [5] have shown that the bifurcation diagram for the two-dimensional Swift-Hohenberg equation is far more complicated, consisting of a lower snaking branch, isolas, and an upper snaking branch.

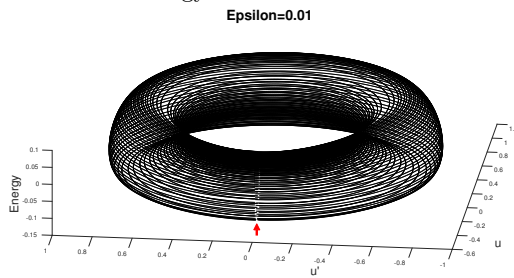


We attempted to better understand the two-dimensional case through a dimensional perturbation to the one-dimensional equation; to do so, we considered radially symmetric solutions to the planar equation, effectively embedding the one-dimensional case into two dimensions. Then, we continuously varied the dimension in a formal sense, letting the dimension, n , be $1 + \varepsilon$ where ε is close to 0. Whereas in the one-dimensional case we were able to restrict our equations to

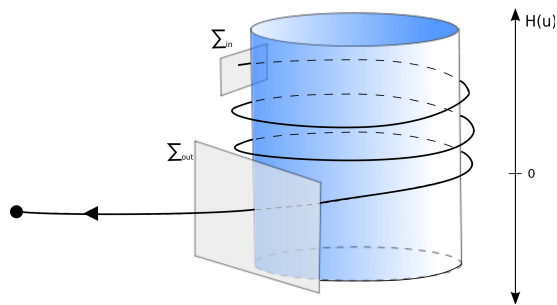
the zero energy level set, this is no longer possible in the $1 + \varepsilon$ -dimensional case. We therefore numerically determined how the energy of our system changes near the periodic orbit that we considered in the one-dimensional case for a small perturbation in the dimension.



From these numerics, we concluded that it is reasonable to assume that the energy of the system decreases. When $\varepsilon = 0$, there is a family of periodic orbits, each with constant energy, that forms a torus. However, when $\varepsilon > 0$, these periodic orbits are no longer constant in energy, thereby creating a torus that is foliated with these new orbits, and the solutions that we care about decrease in energy.



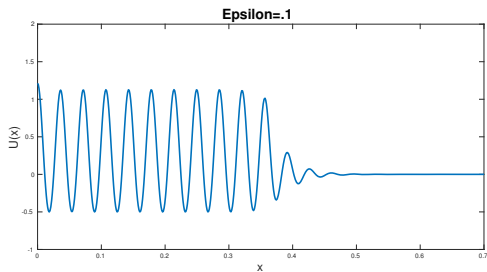
We therefore focused on heteroclinic solutions which start near the torus, spiral down in energy, and converge in forward time to the origin.



^{*}Princeton University
[†]University of California Santa Barbara
[‡]Brown University
[§]Boston University
[¶]Pitzer College



This corresponds to solutions which are nearly periodic near the origin and converge to zero as $x \rightarrow \infty$.



We are able to show that snaking as well as these roll solu-

tions persist in the $\varepsilon > 0$ case, however, because the solutions are no longer constant in energy, there is a limit to the number of times solutions can wind around the torus without falling off. As the number of rolls corresponds to the value of the L^2 -norm, this explains why there is an upper bound for the lower snaking branch. This upper bound changes depending on the value of ε and is very large for small ε . Letting L be this upper bound, we can see that the predicted maximum height of the lower snaking branch is as follows:

$$L = e^{1/\varepsilon} \tag{2}$$

In the future we hope to be able to explain the upper snaking branch and the isolas for $\varepsilon > 0$.



References

- [1] Daniele Avitabile, David JB Lloyd, John Burke, Edgar Knobloch, and Björn Sandstede. To snake or not to snake in the planar swift-hohenberg equation. *SIAM Journal on Applied Dynamical Systems*, 9(3):704–733, 2010.
- [2] Margaret Beck, Jürgen Knobloch, David JB Lloyd, Björn Sandstede, and Thomas Wagenknecht. Snakes, ladders, and isolas of localized patterns. *SIAM Journal on Mathematical Analysis*, 41(3):936–972, 2009.
- [3] David JB Lloyd and Hayley O’Farrell. On localised hotspots of an urban crime model. *Physica D: Nonlinear Phenomena*, 253:23–39, 2013.
- [4] Elizabeth Makrides and Björn Sandstede. Predicting the bifurcation structure of localized snaking patterns. *Physica D: Nonlinear Phenomena*, 268:59–78, 2014.
- [5] Scott McCalla and Björn Sandstede. Snaking of radial solutions of the multi-dimensional swift–hohenberg equation: A numerical study. *Physica D: Nonlinear Phenomena*, 239(16):1581–1592, 2010.
- [6] Ehud Meron. Pattern-formation approach to modelling spatially extended ecosystems. *Ecological Modelling*, 234:70–82, 2012.
- [7] Efrat Sheffer, Hezi Yizhaq, Moshe Shachak, and Ehud Meron. Mechanisms of vegetation-ring formation in water-limited systems. *Journal of theoretical biology*, 273(1):138–146, 2011.

Stability of Agent-based Models: Overview

Cassandra Cole, Philip Doldo, Qing Fan

August 12, 2016

1 Research Goals

The primary goal of our project was to understand the long-term stability of agent-based models, especially the agent-based model of zebrafish pigment cells. In particular, examining the zebrafish model led us to consider agent-based models in which deterministic flow and stochastic processes occur on similar timescales. The methods we used to do this were twofold: we simulated a one-dimensional approximation of the model to gain an intuitive understanding, and we applied previous results on piecewise-deterministic Markov processes to our models to analytically show the existence of a stationary distribution.

2 Methods and Progress

2.1 Numerics

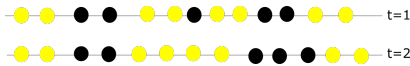


Figure 1: Toy Model in 2 Timesteps

We simulated a one-dimensional model over time (see Figure 1). To simulate deterministic flow, we used ODEs that model cells repelling and attracting each other. For birth and death, times were chosen based on a Poisson process, and locations (for birth) were chosen probabilistically based on the ratios of cells of each color in a given region and in long-range regions around it. For an example of the full simulation, see Figure 2. We were able to create a simulation that leads to “stripes” (or some one-dimensional analog of stripes) even when started with random initial conditions. Additionally, we ran the simulation with only deterministic movement or only birth and death to show that both are necessary for the stable “stripe” pattern to form.

2.2 Analysis

We attempted to adapt the zebrafish model to the framework of a PDMP, which is a family of Markov processes in which deterministic flow (in our case, cell repulsion) is punctuated by random jumps in position or velocity (in our case, changes in cell position model birth and death). We spent a significant portion

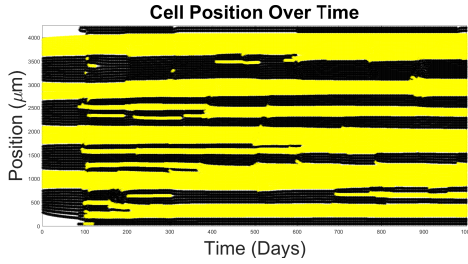


Figure 2: Simulation Over 1000 Days

of the summer attempting to understand the framework and how it is analyzed by Costa (1990), and using Costa's results we were ultimately able to consider models that increasingly approximated the zebrafish model and assess whether or not they fulfilled the criteria for a stationary distribution. We began with simple, relatively trivial models, such as a single cell flowing deterministically and jumping to uniformly random locations within the state space, and ultimately were able to produce results for more realistic systems as outlined in the next section.

3 Results

Our main results involve three increasingly easily satisfied criteria for showing the existence of a stationary distribution (assuming certain necessary assumptions are fulfilled) based on earlier criteria from Costa (1990). We show that, from most general to least general, we can show the existence of a stationary distribution our PDMP satisfies necessary assumptions and:

1. We can write the transition kernel for the Markov chain in terms of some density $\rho_x(y)$ that is defined everywhere in the state space E , and there exists some compact set $\Gamma \subset E$ s.t. $\forall x \in E - \Gamma, \int_{\Gamma} \rho_x(y) dy > 0$, or,
2. We can show that there exists some closed set $\Gamma_0 \subset E$ s.t. $\rho_x(y) < L \forall x, y \in E - \Gamma_0$, or,
3. We can write the transition kernel for the PDMP in terms of some density $\tilde{\rho}_{\phi(x,s)}(y)$ and we can show that $\tilde{\rho}_{\phi(x,s)}(y)$ is defined on E and $0 \leq \tilde{\rho}_x(y) < M < \infty \forall x, y \in E$ and $s \in [0, \infty)$

Using the third result, we analyzed a general system with n cells that flow according to a system of ODEs approximating spring forces and jump simultaneously with uniform probability into intervals with length 2δ around themselves, and we were able to show that this system has a stationary distribution.

4 Future Work

We hope to be able to extend our results to apply to models closer to the full zebrafish model. In particular, we want cell birth locations to be dependent on the locations of other cells and not necessarily on the location of the dying cell,

and we would eventually like to extend the model to include a changing number of cells.

We also hope to extend our research to be able to explicitly calculate stationary distributions for our models, either analytically (if possible) or numerically.

Modelling Stripe Formation on Zebrafish Fins

Madeline Abbott¹, Dorothy Catey², Neil Chandra³,
Francesca Lim³ and Bethany Dubois³

¹Macalester College

²University of Idaho

³Brown University

August 14, 2016

Abstract

Zebrafish are model organisms known for their distinctive horizontal stripes formed by interactions between two types of pigment cells: yellow xanthophores and black melanophores. Our research builds upon an existing agent-based model produced by Volkening and Sandstede that successfully replicates wild type (WT) stripe formation on the zebrafish body. We present a model for the development of WT stripes on the zebrafish caudal fin that incorporates the effects of the fin's bony rays on cell differentiation and migration. We find that stretching the domain primarily in the horizontal direction, restricting cell birth based on the number of like cells surrounding a location, and limiting melanophore birth to bones has the greatest impact on improving our replication of WT stripe formation.

1 Introduction

Zebrafish (*Danio rerio*) are model organisms known for their black stripes and yellow interstripes formed by pigmented cells on the body and fins. The focus of our research is to investigate how inter-cellular interactions lead to the development of WT stripe patterns on the caudal fin.

There are only two types of pigments cells present in the caudal fin: black melanophores and yellow xanthophores. Their interactions are primarily responsible for the formation of patterns on the fin. While the stripes seem to continuously extend, we claim that the underlying mechanisms of pattern formation are different for both the body and the fin based on evidence from mutations that affect stripes on the body but not the fin.

The caudal fin of a young zebrafish initially starts as a paddle shape which eventually transforms into a bi-lobed shape as an adult. The fin grows distally and continuously with the most growth occurring in a zebrafish's first few weeks of life. The fin gains structure from 16-18 bony rays that exhibit saltatory growth, have regenerative properties, and appear to affect melanophore migration.

2 Research Goals

This project is an extension of an existing two-population agent-based model produced by Volkening and Sandstede that successfully replicated WT pattern formation along with mutation and ablation experiments but was unable to model stripes on a caudal fin domain. Therefore the main focus of our research is to successfully model WT pattern formation on the caudal fin by improving the caudal fin domain, implementing cell-bone interactions, and adjusting cell birth, death, and migration rules. We were also interested in replicating several fin mutations such as *leopard* and *long fin*, as well as reproducing fin regeneration experiments. However, we were unable to explore these interests due to time constraints.

3 Domain Modelling

Our model contains a realistic caudal fin domain that incorporates the presence of 18 bony rays. In order to remain true to the biology, we utilized image analysis to trace a smooth outline of a set of developing fin images provided in *Parichy et al. 2009*. We were able to simulate continuous growth of the caudal fin on a day-to-day basis through a transformation process of a sequence of these images.

In order to model possible cell-bone interactions, we included 18 bony rays that grow in proportion to the caudal fin domain. Based on our measurements of fin images from *Parichy et al. 2009*, there is roughly a 3° angle difference between each ray which remains constant throughout fin growth.

4 Major Modifications to Body Code

Initially, we attempted to emulate WT stripe development by altering parameters in the code, such as the number of cells born each day, cell-to-cell forces, and creating new initial conditions to represent the fin pattern at different stages during zebrafish development. Unfortunately these changes proved to be unsuccessful.

Melanophore Migration and Differentiation

Examining images of developing WT and mutant zebrafish fins lead us to infer that the locations of the bony rays affect melanophore differentiation and migration. Therefore, we implemented rules that restricted melanophore differentiation and migration to the bone vectors to varying degrees. The most effective combination we discovered involved melanophores differentiating only along bones but migrating freely.

Stretching Domain

After working with a non-stretching domain for most of the summer, we recently implemented a function that updates the cell positions by stretching every day as the domain grows. Preliminary functions stretched the cells radially from an origin along the proximal edge or along bone vectors, but the most effective model accounts for the nonlinear domain growth by multiplying the

cell positions by a decaying scaling vector that favors horizontal rather than vertical growth.

Increasing Stability of Random Birth

The original model evaluated possible locations for cell differentiation based on overcrowding and melanophore and xanthophore proportions. We added a parameter called “undercrowding” that ensures that if a cell is born, a certain number of other cells must be present locally. This condition prevents patterns from emerging in the lobes around a cluster of randomly differentiated cells and spreading proximally. WT development observes patterns originating at the base of the fin and spreading distally with randomly distributed cells in the most distal regions. This “undercrowding” parameter replicates these trends.

5 Most Recent Result

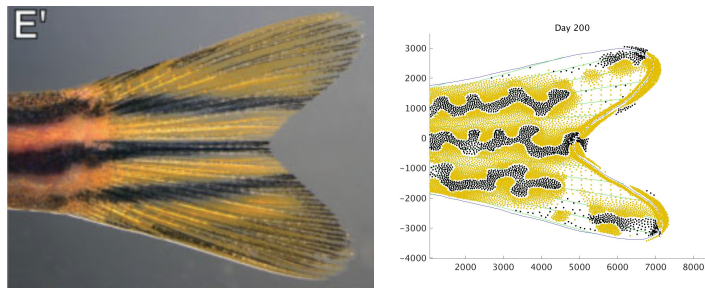


Figure 1: **Day 200:** Comparison of fin image (Parichy 2009) at SL26 and simulation results. Simulation was run from day 33 to day 200 on a growing domain. The fin was initialized with one full length center black stripe surrounded by partial length black stripes on either side. The rest of the fin was densely covered with yellow cells. Black cells were born only on the bones but allowed to migrate in any direction. Note the horizontal yet meandering directionality of the black stripes.

6 Future Work

Though promising, our work this summer is far from complete. This project can be continued through further investigations of the following topics:

1. **Melanophore Migration** Inspection of images causes us to believe that the locations of the bony rays affects the movement of melanophores. We are interested in testing many more potential mechanisms that explain this interaction.
2. **Melanophore Populations** Genetic research on mutated genes such as the *kit* and *fms* indicates that there are multiple pathways for melanophore migration. Treating these different differentiation pathways as different populations of cells could be beneficial to future models.
3. **Independent Xanthophore Patterning** Photos of the melanophore-lacking *nacre* mutants indicate that even in the absence of melanophores,

xanthophores exhibit a spatially dependent pattern. These yellow cells tend to differentiate and migrate only along the dorsal and ventral ends of the fin, with large clusters at the dorsal and ventral ends of the fin base. In contrast, the xanthophore-lacking *pfeffer* mutation shows spatial uniformity in melanophore population on the fin. Currently, the model does not account for these phenomena.

4. **Timescale Adjustment** We are interested in further tuning the timescale in the domain development and cell birth and death. Currently our time scale is based off of measurements from *Parichy et al. 2009*. We believe that more cycles of birth and death each day may contribute to patterns developing more accurately and a larger cell population in the domain.
5. **Data Aggregation** Currently, all the data the model was collected from a limited set of photographs of WT development, mostly published in *Parichy et al. 2009*. More images, especially incrementally between SL 10 and SL 16, would give us key insight into how patterns develop and go far in informing our model. Our domain could then be based more accurately on *average* fin size and growth rates.